

PRECIPITATION OF MAGNESIUM SILICATE HYDRATES IN NATURAL ALKALINE SURFACE ENVIRONMENTS

YUTO NISHIKI^a, TSUTOMU SATO^{b,*}, TAKAYUKI KATOH^c,
TSUBASA OTAKE^b, AND RYOSUKE KIKUCHI^b

^aGraduate School of Engineering, Hokkaido University,
Kita 13, Nishi 8, Kita-ku, Sapporo, Hokkaido 060–8628, Japan

^bFaculty of Engineering, Hokkaido University, Kita 13, Nishi 8, Kita-ku, Sapporo, Hokkaido 060–8628, Japan

^cEarth Science Co., Ltd., 2–1, Kita 39, Nishi 3, Kita-ku, Sapporo, Hokkaido 001–0039, Japan

(Received December 20, 2019. Accepted February 17, 2020)

ABSTRACT

Magnesium silicate hydrate (M–S–H) has been considered to play a significant role in different fields of engineering geology including radioactive waste disposal and geological storage of CO₂. However, M–S–H has been discussed only with synthetic samples in most previous studies. To confirm and characterize M–S–H precipitated in natural surface environments, and to assess the formation conditions and processes of the M–S–H, we investigated present-day precipitation of M–S–H at an ultramafic body in the Kamuikotan tectonic belt, Hokkaido, Japan. We collected seepage, surface water, and surface sediments on the ultramafic rock mass. Seepage and surface water showed alkaline pH and Mg²⁺–HCO₃[–] type water. Although bulk XRD analysis of the sediments did not clearly identify peaks of M–S–H due to its low crystallinity, microscopic observation showed that the sediments contained solid phases that are precipitated interstitially around the detrital serpentine particles. A TEM analysis identified the phases as M–S–H that may be mineralogically considered as a low-crystalline chrysotile with nano-tubular morphology. Thermodynamic calculations for the collected liquid samples suggest that mixed solution of seepage and surface water having high Si activity can induce the formation of M–S–H. The precipitation of M–S–H is likely to be a commonly occurring phenomenon in natural Mg–Si–H₂O systems where geochemical environments contain alkaline fluid that shows high Si activity and meets the thermodynamic conditions for M–S–H formation. In addition to the precipitation of M–S–H in Mg–Si–H₂O systems, we also observed that M–S–H is precipitated even under conditions including Ca and CO₂ species (i.e., Mg–Ca–Si–CO₂–H₂O systems), with a simultaneous precipitation of aragonite. This study supports an understanding of the precipitation of M–S–H by mineral–water interactions in natural surface/subsurface environments for various engineering geology fields.

Key words: alkaline condition, carbon dioxide capture and storage, chrysotile, magnesium silicate hydrate (M–S–H), mineral–water interaction, radioactive waste disposal, natural analogue, serpentine, serpentinization

INTRODUCTION

Precipitation of low-crystalline clay minerals is an important issue in discussions of mineral–water interaction in surface/subsurface geology because low-crystalline phases easily form at ambient temperatures. Among these, allophone and imogolite are low-crystalline clay minerals (aluminum silicate hydrates) precipitated with mineral–water interactions in Al–Si–H₂O systems, which have been studied extensively.

They are generated by weathering of volcanic ash and have high adsorption capacities for foreign ions (Wada, 1989). Further, recently magnesium silicate hydrate (M–S–H: defined as low-crystalline material composed of magnesium, silica, and water in this paper) is also being discussed actively in several fields of engineering geology evaluating mineral–water interactions in Mg–Si–H₂O systems under alkaline conditions. For instance, formation of the M–S–H will be a key issue in geological storage of CO₂ (Okamoto *et al.*, 2006; Ninomiya *et al.*, 2007), radioactive waste disposal (Ramirez *et al.*, 2002; Mäder *et al.*, 2017), chemical enhanced oil recovery (Umar and Saaid, 2013; Olajire, 2014), immobilization of contaminated soil (Nozawa *et al.*, 2018), and treatment of contaminated water (Zhuang *et al.*, 2009). In addition to study in engineering fields, experimental investigations of M–S–H

*Corresponding author: Tsutomu Sato, Faculty of Engineering, Hokkaido University, Kita 13, Nishi 8, Kita-ku, Sapporo, Hokkaido 060–8628, Japan. e-mail: tomsato@eng.hokudai.ac.jp

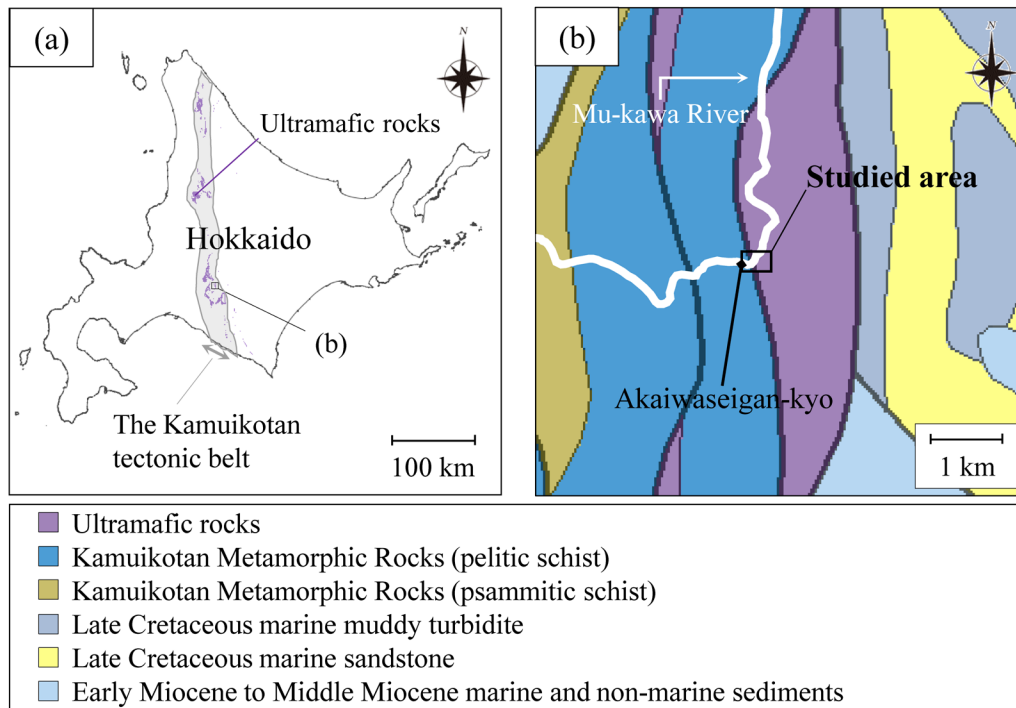


Fig. 1. Geological setting around the Kamuikotan tectonic belt in Hokkaido, Japan (after Geological survey of Japan, 2019). (a) Distribution of ultramafic rocks in the Kamuikotan tectonic belt; (b) geological map around studied area.

has been performed as a basic study on sedimentology and geochemistry of lacustrine and peri-marine environments (Tosca and Masterson, 2014).

Although much research has been performed on M–S–H, most previous reports have discussed only experimental results. For instance, Roosz *et al.* (2015) and Nied *et al.* (2016) analyzed laboratory synthetic M–S–H samples. The reported M–S–H was poorly crystalline and crystallographic identifications were difficult. The results of those structural analyses suggested that M–S–H is disordered and is a defective layered silicate somewhat similar to talc or serpentine, a conclusion which is, however, still not commonly accepted and has not been clearly confirmed.

There are few studies related to observation of natural M–S–H samples even when M–S–H is essentially thought to form in natural surface/subsurface environments. Research of such situations with M–S–H has probably been avoided due to the low crystallinity of M–S–H. In recent years, de Ruiter and Austrheim (2018) reported the formation of M–S–H cement in an ultramafic complex in the presence of quartz-rich felsic glacial deposits. However, further mineralogical analyses are required to characterize the M–S–H here, and there were no details of observations and analysis of the fluid that leads to the M–S–H formation. Milodowski *et al.* (2016) and Shimbashi *et al.* (2018) observed secondary formed clay minerals where alkaline ground water was flowing. Although those minerals were essentially Mg–silicate clay minerals, they contained as much Al and Fe as Mg.

In this context, there are still insufficient mineralogical and geochemical studies on the M–S–H formation in natural settings. Therefore, we investigated present-day natural precipitation of M–S–H to confirm and characterize the M–S–H precipitated in natural alkaline surface environments, and as-

sess the formation conditions and processes of M–S–H.

GEOLOGICAL SETTING AND SAMPLES

In order to observe present-day precipitation of M–S–H under natural alkaline conditions, we focused on a geological setting with (ultra)mafic rock and water.

Ultramafic rock is found in various regions around the Kamuikotan tectonic belt in Hokkaido, which is one of the Japanese islands (Figure 1a). The Kamuikotan tectonic belt is characterized by zones of ultramafic rock running north-south intermittently and identified as a typical high-pressure/low-temperature metamorphic belt from the late Mesozoic age (Asahina and Komatsu, 1979). Ueda (2005) described subduction zone tectonics to demonstrate the formation of the Kamuikotan tectonic belt. Due to tectonic interaction between the Eurasian plate and an oceanic plate in the Cretaceous period (before formation of the current Japanese islands including Hokkaido), ophiolite (lower Sorachi ophiolite) was being uplifted, while metamorphosing with Cretaceous accretionary complexes. The ophiolite is largely composed of mafic rock (MORB-like tholeiite) and ultramafic rock (serpentinized peridotite), so that ultramafic rock is observed in the Kamuikotan tectonic belt with crystalline schists and Cretaceous sedimentary rock. In the ultramafic rock, there are few fresh peridotites unaffected by serpentinization (Asahina and Komatsu, 1979). Serpentinite mélange and turbidite are commonly observed in the Kamuikotan tectonic belt as a result of the subduction zone tectonics (Katoh and Nakagawa, 1986; Ueda, 2005).

The samples analyzed in this study were collected from one of the ultramafic regions within the Kamuikotan tectonic belt (Figure 1b). The studied area is located near Akaiwaseigan-

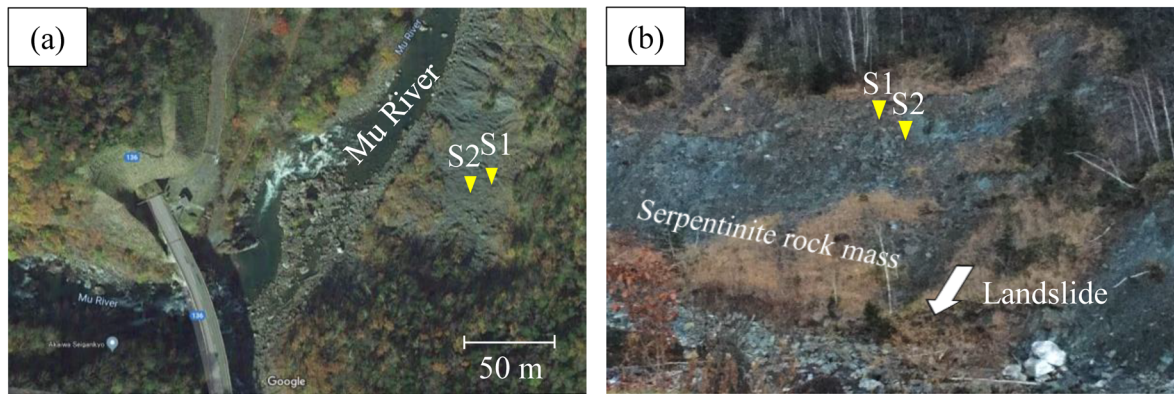


Fig. 2. Photographs showing location of sampling sites (S1 and S2). (a) Overhead view of the studied area (after Google); (b) photograph of an ultramafic rock mass and the sampling sites.

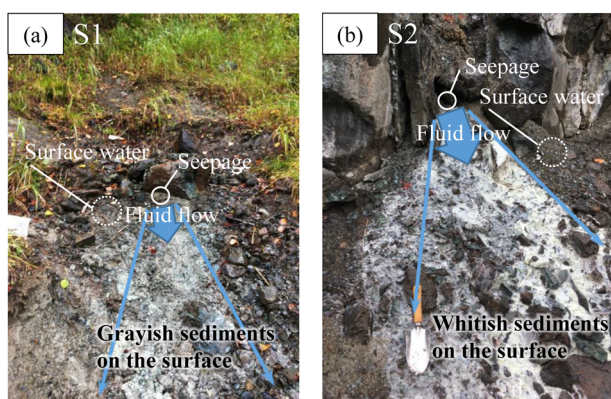


Fig. 3. Photographs of the sampling sites: (a) S1 and (b) S2.



Fig. 4. Photograph of serpentine veins.

kyo, a gorge consisting of red chert and metamorphosed tuff. Ultramafic rock here is mainly serpentinite that was originally harzburgite and dunite with a small amount of lherzolite (Katoh and Nakagawa, 1986). The fresh serpentinite rock and its crushed sediments are observed on the surface in the studied area due to landslides (Figure 2). Samples were collected from two specific sites, S1 and S2, where seepage was flowing from the surface of the ultramafic rock mass. Grayish and whitish sediments were observed on the surface around the seepages in S1 and S2, respectively (Figure 3). We collected surface waters around the sediments, seepage waters, and the surface sediments, which were aggregates of grains bound to each other due to cementation. In addition, a fragment of bedrock was collected to compare the characteristics of the sediments with those of the bedrock in and around this area. Typical serpentine veins were observed in some rocks (Figure 4), and only the minerals composing the serpentine veins were removed and collected for the analyses.

ANALYTICAL METHODS

Solution analyses

The pH and oxidation reduction potential (ORP) of the liquid samples were measured on site by electrodes (pH: 9625-10D; Eh: 9300-10D, Horiba, Ltd.) and meters (pH: LAQUAact D-74; ORP: LAQUAact D-75, Horiba, Ltd.). The ORP values were measured by an Ag/AgCl electrode with 3.33 mmol/L KCl and corrected using the following equation

(Matsushita *et al.*, 1974):

$$Eh = ORP_{Ag/AgCl} + 206 - 0.7 \times (T - 25),$$

where Eh is an ORP value measured by a standard hydrogen electrode (mV), $ORP_{Ag/AgCl}$ is an ORP value measured by the Ag/AgCl electrode (mV), and T is the temperature ($^{\circ}C$). Alkalinities were measured by titrating HNO_3 (Kanto Chemical Co., Inc.) into 50 mL of liquid samples that had been filtered through 0.45 μm polytetrafluoroethylene (PTFE) membrane filters (Advantec Co., Ltd.). The Inflection Point Titration method (Rounds, 2012) was applied to obtain the alkalinities and the concentrations of HCO_3^- and CO_3^{2-} .

To analyze major cations and anions other than H^+/OH^- and HCO_3^-/CO_3^{2-} , the collected liquid samples were filtered through 0.2 μm and 0.45 μm PTFE membrane filters (Advantec Co., Ltd.), respectively. In addition, and only for analysis of major cations, the filtered solutions were acidified by 1 vol% HNO_3 (Kanto Chemical Co., Inc.). After the liquid samples were brought back to the laboratory, concentrations of the cations were determined by inductively coupled plasma atomic emission spectroscopy (ICP-AES; ICPE-9000, Shimadzu Corp.), and those of the anions were determined by ion chromatography (IC; 861 Advanced Compact IC, Metrohm AG). "ICP multi-element standard solution IV" (Merck KGaA) and "Anion Mixture Standard Solution 1" (FUJIFILM Wako Pure Chemical Corp.) were used as the calibration standards, respectively. The concentration of dissolved Si was also determined by ICP-AES with "Silicon Standard Solution"

Table 1. On-site measurements of the surface waters from S1 and S2 (S1-sf and S2-sf) and the seepage waters from S1 and S2 (S1-sp and S2-sp), and their concentrations of major cations and anions.

Sample		S1-sf	S2-sf	S1-sp	S2-sp
pH	—	9.69	9.58	10.34	10.67
Eh	mV	410	397	377	361
Na	mg/L	1.62	1.72	1.88	1.96
K	mg/L	0.244	0.269	0.219	0.279
Mg	mg/L	18.4	15.3	24.4	13.7
Ca	mg/L	1.31	3.44	1.38	10.4
Si	mg/L	0.083	0.008	0.112	0.009
Cl ⁻	mg/L	5.91	19.3	5.54	17.5
SO ₄ ²⁻	mg/L	1.48	0.60	4.27	<0.03
NO ₃ ⁻	mg/L	1.18	1.08	2.82	2.91
NO ₂ ⁻	mg/L	1.10	<0.02	<0.02	<0.02
alkalinity	mg/L as CaCO ₃	100.1	69.7	108.1	70.5
HCO ₃ ⁻	mg/L	79.2	60.7	54.9	18.0
CO ₃ ²⁻	mg/L	19.7	10.9	33.9	24.8

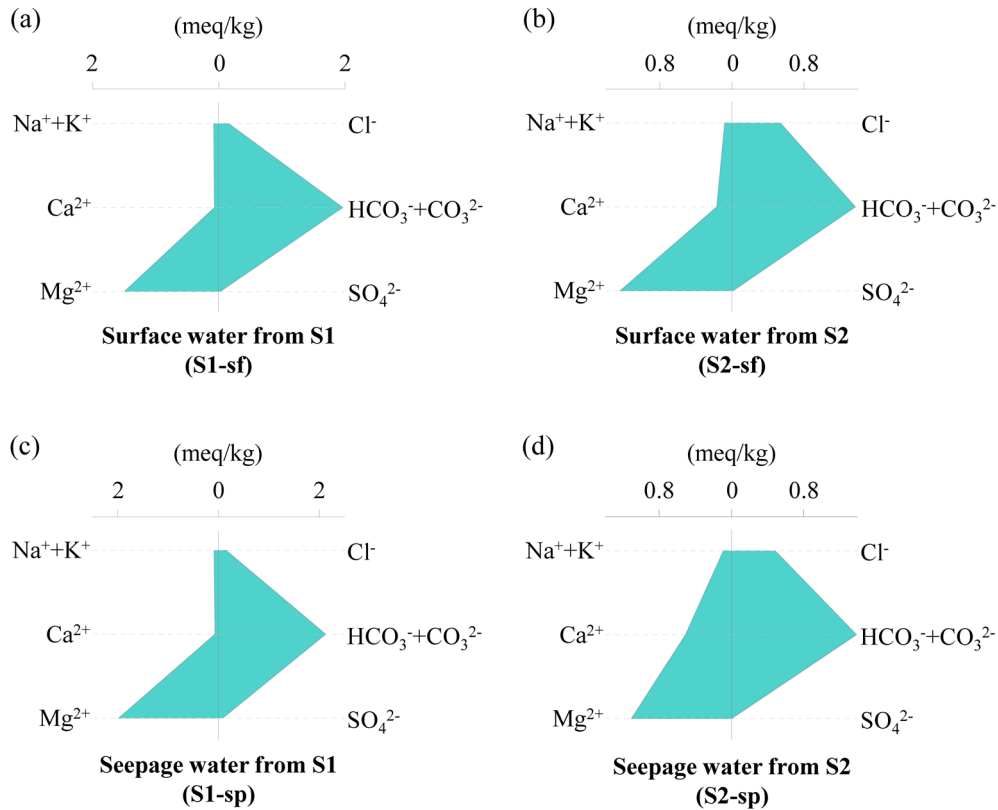


Fig. 5. Stiff diagrams showing the water chemistry of (a) surface water from S1, (b) surface water from S2, (c) seepage water from S1, and (d) seepage water from S2, which are obtained from Table 1.

(FUJIFILM Wako Pure Chemical Corp.).

Solid analyses

The sediments and rock samples were air-dried for the solid analyses. Both samples were crushed with an agate mortar for powder X-ray diffraction (XRD) analysis to determine bulk mineralogy of the samples. An X-ray diffractometer (RINT-2100, Rigaku Corp.) was operated at 30 kV and 20 mA and equipped with a Cu target. Randomly oriented powder samples were scanned from 2 to 70° 2θ at a scanning speed of 1°/min.

Polished sections of sediment samples were made by a method patented by Owada *et al.* (2014) to observe the microstructure of sediments. Conventional methods for making petrographic sections are not suitable for unstable specimens such as clay because petrographic structures of clayey samples are ordinarily broken during polishing of the samples by water or oil, where these liquids protect the samples from the heat generated during the cutting and grinding processes. However, the method developed by Owada *et al.* (2014) does not require liquid addition and frictional heat is minimized, so that samples are not influenced by the liquids or heating.

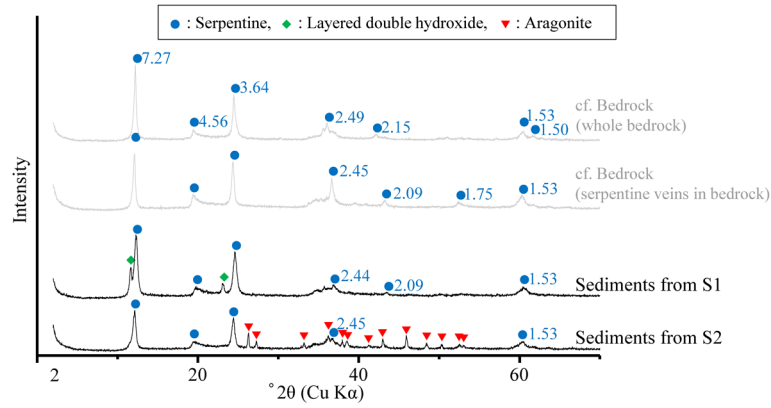


Fig. 6. XRD patterns of collected sediments and bedrock. Peak positions of serpentine are displayed as *d*-values (Å).

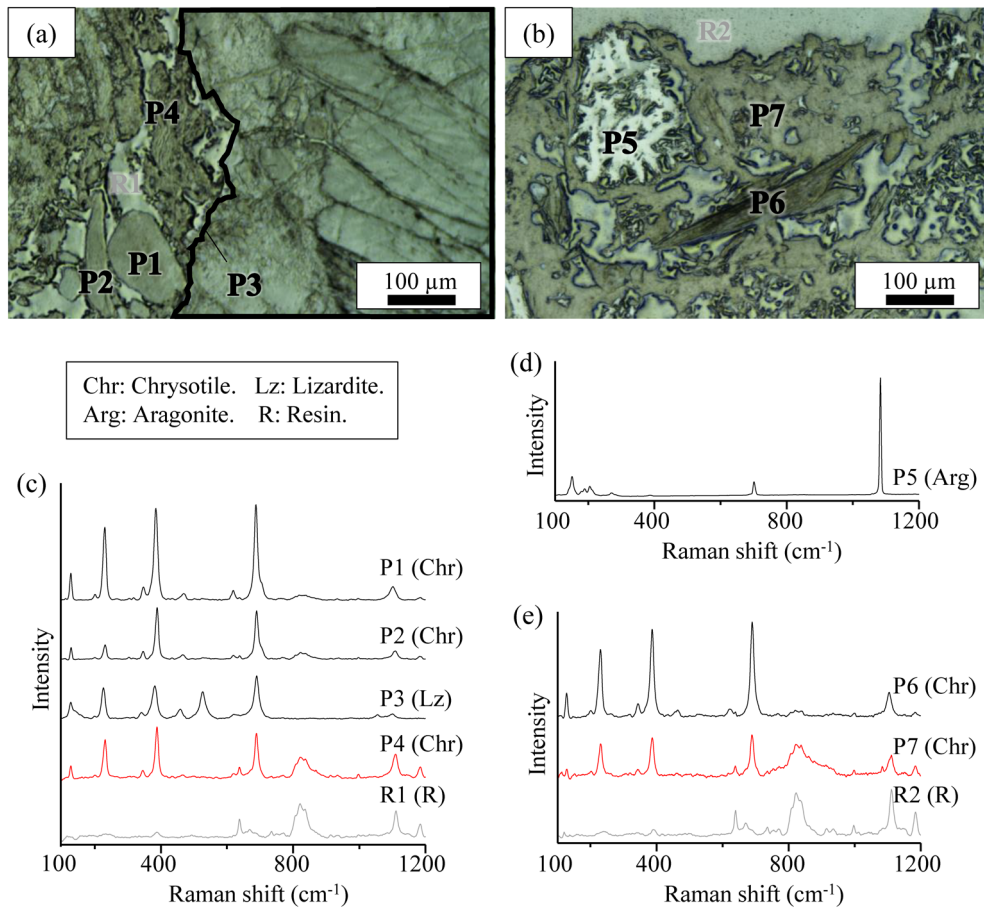


Fig. 7. Microanalyses of collected sediments. (a) Optical microscopic image of a section showing a lump of sediments from S1; (b) optical microscopic image of a section showing a lump of sediments from S2; (c) Raman spectra of P1–P4 and R1 in (a); (d) Raman spectrum of P5 in (b); (e) Raman spectra of P6, P7, and R2 in (b).

The collected sediment samples in this study are clayey cemented aggregates, and the Owada *et al.* method retains the sedimented form of the sample during the polishing.

The occurrence of precipitates was observed by optical microscopy (BX60, Olympus Corp.) with reflected light. To mineralogically identify particles composing the sediments, micro-Raman spectroscopy (XploRA, Horiba, Ltd.) was applied. Micro-Raman spectroscopy is a powerful tool to identify mineral particles of the micrometer scale, distinguishing polymorphs. We referred to previous studies by Rinaudo *et al.* (2003) for identifying the serpentine minerals (chrysotile, liz-

ardite, and antigorite), and Kontoyannis and Vagenas (2000) for identifying Ca-carbonate polymorphs (calcite, aragonite, and vaterite). During the analysis, Raman spectra were obtained using a 532-nm laser, at a 2400 grooves per millimeter grating, 100 μm confocal hole diameter, and 100 μm slit size. The spectral acquisition time was 20 s and data for 3 spectra were recorded for each sample. The system was calibrated with a silicon standard.

Some of solid phases in the polished sections were observed in further detail by transmission electron microscopy (TEM) to discuss the morphology at the nanometer scale, the

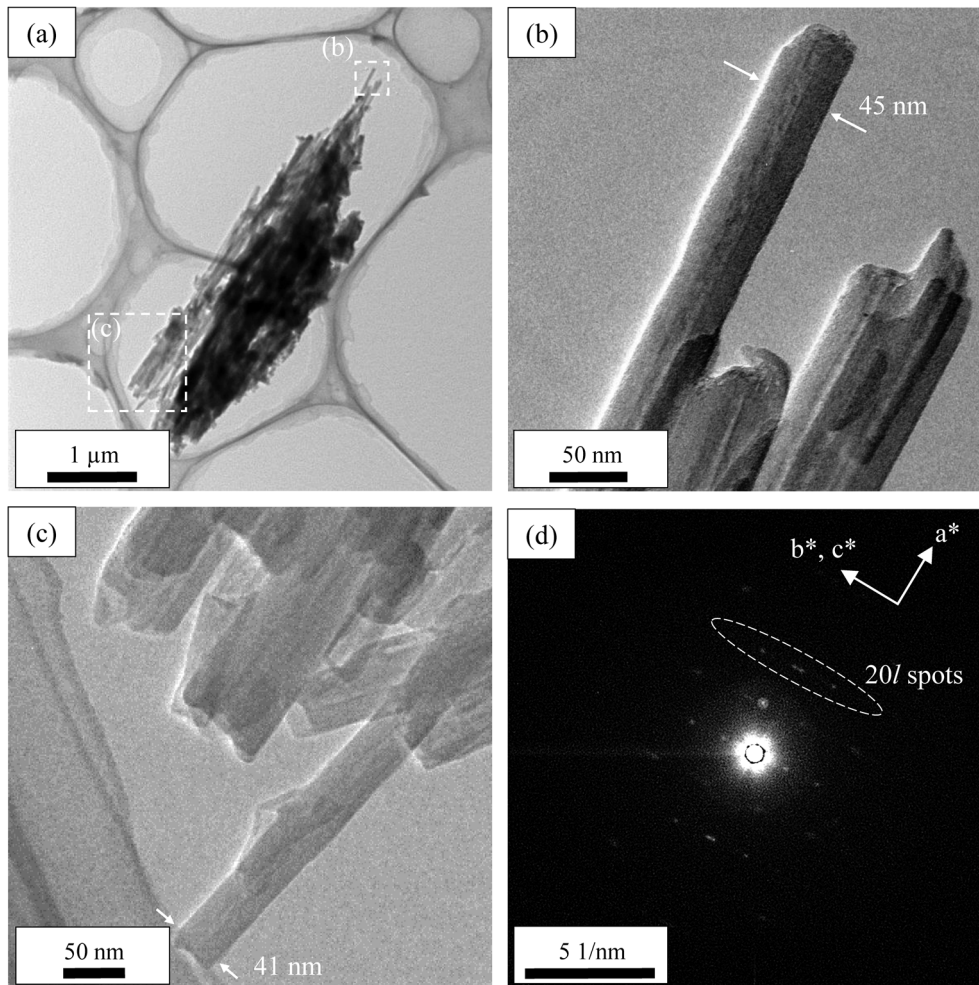


Fig. 8. TEM results of particles composing the bedrock. (a) TEM image of representative particles; (b), (c) high magnification images of the areas displayed by dotted lines in (a); (d) SAED pattern of the area in (b).

crystallinity, and chemical composition of the phases. These specimens were picked out by a micromanipulator (Quick Pro, Micro Support Co., Ltd.) and a hard tool probe (TP-005, Micro Support Co., Ltd.), and placed on copper grids with carbon films (Microgrid type A, Okenshoji Co., Ltd.). They were analyzed transmission electron microscopically (JEM-2010, JEOL Ltd.) at an operating voltage of 200 kV. An energy dispersive X-ray spectroscope (EDS) attached to the TEM was also used to determine the chemical compositions of the minerals. Particles composing the serpentine veins in the rock (Figure 4) were also observed by TEM for comparison with the picked out phases from the sediment sections. Before the TEM observations, powdered samples from serpentine veins were dispersed in ethanol and one drop of the sample suspension was deposited on the grids.

RESULTS

Water chemistry

Table 1 shows the water chemistry of the liquid samples: surface waters from S1 (S1-sf) and S2 (S2-sf), and seepage waters from S1 (S1-sp) and S2 (S2-sp). The pH values of all the water samples were alkaline, and the pH values of seepage water samples (~ 10.5) were higher than those of the surface water samples (~ 9.5). The Eh values of all samples

were somewhat high (~ 400 mV), indicating oxidized aquatic environments. The ICP-AES analysis showed that the liquid samples contained detectable concentrations of Na, K, Mg, Ca, and Si. In terms of anions, the IC analysis showed concentrations of Cl^- , SO_4^{2-} , and $\text{NO}_3^-/\text{NO}_2^-$, and the alkalinity measurements indicated concentrations of $\text{HCO}_3^-/\text{CO}_3^{2-}$. Combining the results of the concentrations of cations and anions, the calculated charge imbalances were within $\pm 14\%$ for all the liquid samples. Stiff diagrams of the water chemistry show that major chemical compositions of S1-sf, S2-sf, S1-sp and S2-sp were similar, dominated by Mg^{2+} and $\text{HCO}_3^-/\text{CO}_3^{2-}$ (Figure 5). Particularly the S2-sp contained slightly higher Ca concentration than the other samples.

Bulk mineralogy

The XRD profiles of all the bedrock samples (whole bedrock and veins in the bedrock; Figure 4) and sediments from S1 and S2 showed that they were dominated by peaks for serpentine (Figure 6). Whereas some peaks for serpentine ($d \approx 7.27, 4.56, 3.64,$ and 1.53 \AA) were observed in all the samples, other peaks for serpentine were observed at a variety of positions among the samples originating in different species of serpentine (chrysotile, lizardite, and antigorite). The XRD profile of the whole bedrock samples indicated lizardite, and that of the vein samples indicated chrysotile. No peaks for

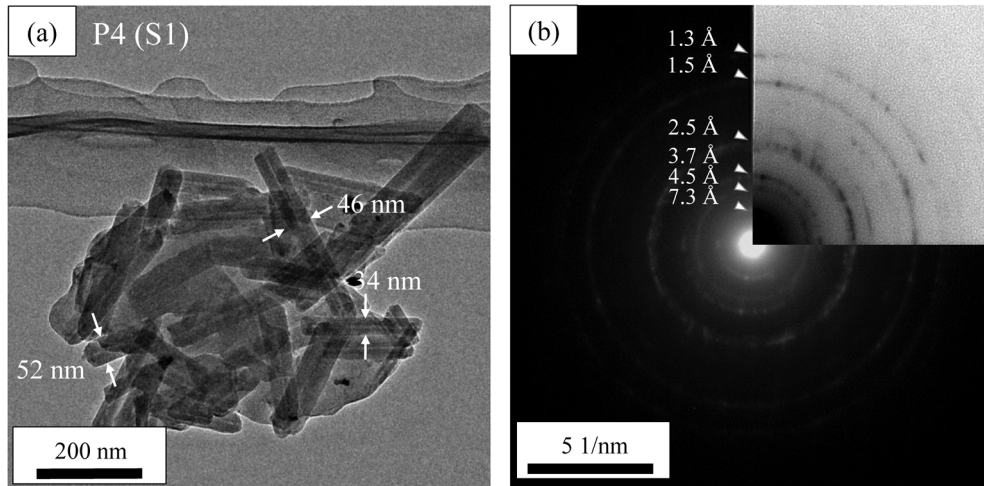


Fig. 9. TEM results of P4 in Fig. 7a. (a) TEM image of observed particles; (b) SAED pattern of the area in (a).

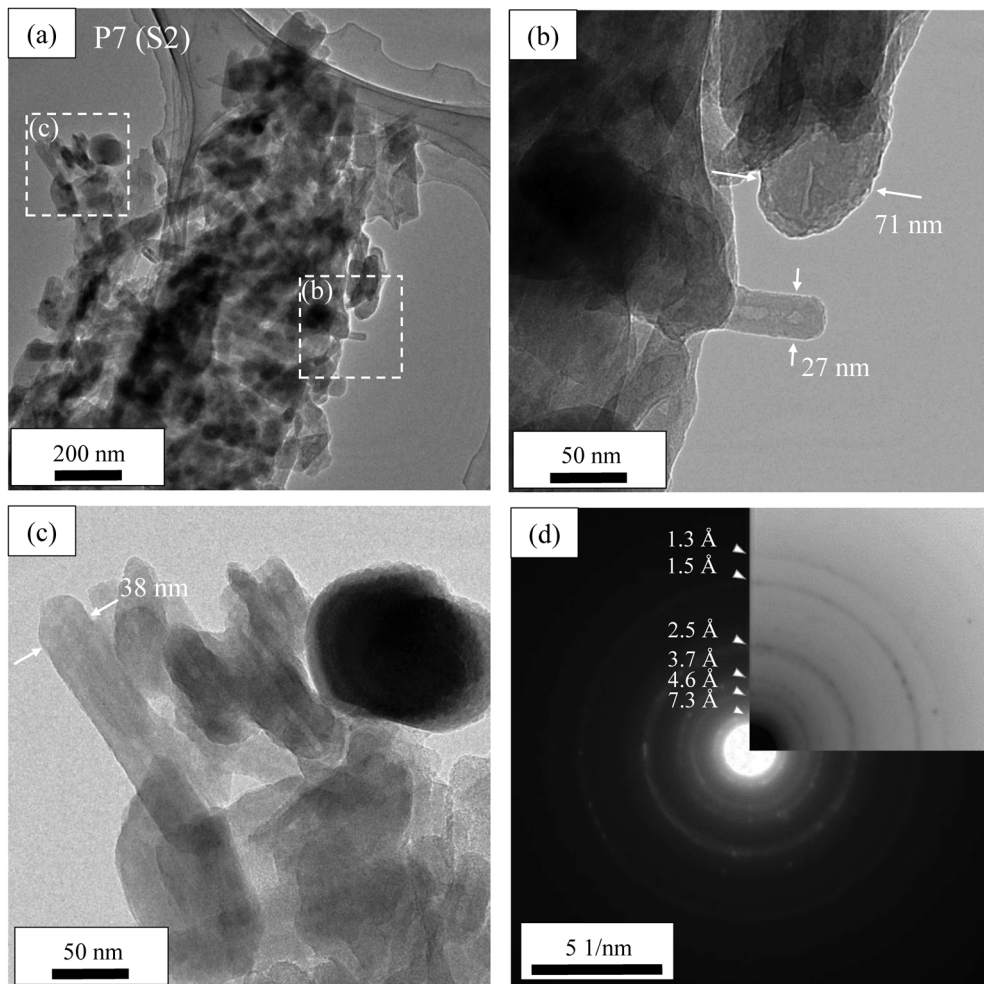


Fig. 10. TEM results of P7 in Fig. 7b. (a) TEM image of representative particles; (b), (c) high magnification images of the areas displayed by dotted lines in (a); (d) SAED pattern of the area in (a).

antigorite were identified in either sample. Serpentine species in the sediment samples are impossible to distinguish only in XRD profiles because the intensities of peaks other than $d \approx 7.27$, 4.56, 3.64, and 1.53 Å are too low to be identified.

Other than serpentine, there were no peaks for minerals generally composing ultramafic rock (olivine, pyroxene, etc.) or for byproducts arising from the serpentinization process

(brucite, magnetite, etc.) in any of the samples, suggesting that the collected bedrock samples are serpentinite mainly composed of just serpentines (chrysotile and lizardite).

Sediment samples from S1 and S2 also showed peaks for hydroxalite-like layered double hydroxide (LDH) and aragonite, respectively. The presence of M-S-H was not clearly shown in the samples although M-S-H synthesized

in previous studies has broad humps around 4.51, 3.34, 2.56, and 1.54 Å in the XRD profiles (Roosz *et al.*, 2015; Nied *et al.*, 2016).

Microscopic observation and micro-Raman spectroscopy

A polished section of sediment from S1 was observed by optical microscope, and the results showed rounded grains (P1 and P2) and a scale-like grain (P3) (Figure 7a). In addition, a solid phase with ambiguous morphology (P4) was observed around the grains (i.e., P1, P2, and P3). Microscopic observation of the sediment from S2 showed an aggregate (P5) of fine needle-like grains and a rod-like grain (P6) (Figure 7b), also here there was a solid phase of ambiguous morphology (P7) around the grains (i.e., P5 and P6). Here it is noteworthy that P4 and P7 bind the grains in S1 and S2, respectively, and other than in Figure 7a and b, this kind of solid phase was also commonly observed around grains in the polished sections.

Micro-Raman spectroscopy was used to determine the mineralogy of the particles in the sediments, identifying P1, P2, P4, P6, and P7 as chrysotile, P3 as lizardite, and P5 as aragonite (Figure 7c–e). The chrysotile identified in P1, P2, P4, P6, and P7 showed Raman spectra with similar peaks, excluding the effect of resin. However, given the morphology and texture of the phases, P4 and P7 must be considered to be different from P1, P2, and P6 as they do not have well defined shapes.

Transmission electron microscopy

The TEM observations of chrysotile crystals from the bedrock samples showed that they are of tubular shape (length >1 μm, Figure 8a; width ~43 nm, Figure 8b, c). The selected area electron diffraction (SAED) pattern of one of the tubular crystals showed typical diffraction spots of chrysotile (Figure 8d). Strictly, the identified chrysotile was determined as clino-chrysotile because 20 l spots are not diffracted at even intervals, following TEM studies on serpentine minerals by Zussman *et al.* (1957) and Yada (1979).

The P4 and P7 in the polished section (Figure 7a, b) were picked out by a micromanipulator for the TEM observations. The P4 was an aggregate of nano-tubes (length ≈ 500 nm; width ~30–50 nm) with some indeterminate components (Figure 9a). A SAED pattern of the aggregate of particles showed six diffuse rings (Figure 9b), indicating that the particles consisted of poly- and low-crystalline minerals. The d -values of these were 7.3, 4.5, 3.7, 2.5, 1.5, and 1.3 Å, which is consistent with those of chrysotile. The P7 were also an aggregate of nano-tubular particles and indeterminate components (Figure 10a). Observation with higher magnification showed that the tubular particles have various widths (~30–~70 nm; Figure 10b, c). The tube length of particles composing P7 was much shorter than that of the chrysotile from the bedrock. The SAED pattern of the aggregate of P7 was also similar to that of P4 (Figure 10d). The above results indicate that P4 and P7 are low-crystalline chrysotile and that they have similar characteristics, completely different from the chrysotile composing bedrock.

During the TEM observations, EDS spectra were obtained on the above particles. All the EDS spectra had peaks related to C, O, Mg, Si, Fe, and Cu (Figure 11). Because the samples

were placed on copper grids coated with carbon films, the EDS spectra demonstrate that the chrysotile from the bedrock, P4, and P7 were mainly composed of Mg, Si, and O with a small amount of Fe. There were no significant differences in the chemical compositions among the three above samples.

DISCUSSION

Characteristics of minerals in the bedrock

Minerals composing the bedrock in the studied area are mainly chrysotile and lizardite, which was demonstrated by the XRD analysis (Figure 6). Katoh and Nakagawa (1986) reported that the major serpentines in the ultramafic rock around the Kamuikotan tectonic belt are chrysotile and lizardite, not antigorite, based on a geologic survey throughout the belt, and this is consistent with the findings of this study.

The chrysotile in the bedrock was characterized in detail by TEM. In general, chrysotile crystals have a cylindrical and tubular structure of 22–65 nm width (Wicks and O’Hanley, 1988). Chrysotile is commonly composed of Mg, Si and O/OH with some substitutions by other elements such as Al, Fe, and Ni (Wicks and O’Hanley, 1988). Given polytypes of chrysotile, chrysotile formed in harzburgite or dunite is generally clino-chrysotile rather than ortho-chrysotile (O’Hanley, 1996). The above characteristics of chrysotile are consistent with those determined in this study (Figures 8 and 11a), which demonstrates that the chrysotile we observed in this study is a quite common chrysotile.

Formation of magnesium silicate hydrates

Discussing the several analytical results of sediment samples, this section establishes that the sediment samples here

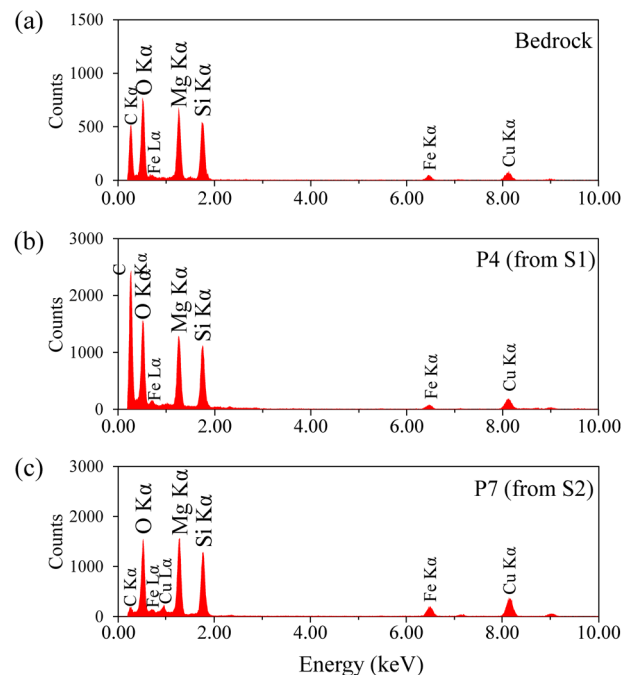


Fig. 11. EDS results obtained during TEM observations. (a) EDS spectrum of particles composing the bedrock in Fig. 8a; (b) EDS spectrum of P4 in Fig. 9a; (c) EDS spectrum of P7 in Fig. 10a.

contain solid phases precipitated on the surface of serpentine, and that some of the phases are M–S–H.

Bulk XRD analysis indicates that the sediment samples from S1 and S2 contain serpentine with LDH and aragonite, respectively (Figure 6). Considering that the XRD profiles of the bedrock samples do not have peaks for LDH and aragonite, the LDH and aragonite would be precipitated at the sites. Precipitation of M–S–H is not clearly identified in the XRD profiles of the sediment samples. However, the intensities of the peaks for serpentine (esp. peaks other than at $d \approx 7.27$, 4.56, 3.64, and 1.53 Å) are lower than those of the bedrock samples. This invites the suggestion that sediment samples may also contain low-crystalline precipitates, and that the broad peaks of the low-crystalline precipitates may be overlapping peaks of crystalline serpentine.

The precipitates were observed in the sediment samples by microscopy and mineralogically identified by micro-Raman spectroscopy. Some solid phases with ambiguous morphologies (P4 and P7; Figure 7a, b) are observed around grains with more clearly defined shapes (P1, P2, P3, P5 and P6; Figure 7a, b), and these phases bind the grains together. Therefore, the sediment samples may be assigned as cemented aggregate of grains formed on site. The micro-Raman spectroscopy identified P1, P2, P3, P4, P6, and P7 as chrysotile or lizardite (Figure 7c, e). Considering the above characteristics of the sediment samples, the mineralogy of the bedrock samples (detailed in the previous section), and the geological setting of the sites, we wish to assign P1, P2, P3, and P6 to be detrital grains from the bedrock, and P4 and P7 as precipitated phases although all of P1, P2, P3, P4, P6, and P7 show similar Raman spectra. Taken together, the various results make it appear that P4 and P7 are precipitated interstitially around the detrital serpentine particles.

Further characterization of the precipitated phases (P4 and P7) was performed by TEM. The P4 and P7 are aggregates of indeterminate components with the nano-tubular crystals. The tube lengths are much shorter than that of usual chrysotile (Figures 8a, 9a, and 10a), and the width varies around ~ 30 – ~ 70 nm (Figures 9a, 10b, c). The SAED patterns show diffuse rings, and the d -values are consistent with chrysotile (Figures 9b and 10d). Taken together, the above characteristics suggest that P4 and P7 are chrysotile, but low-crystalline and not highly ordered phases. Additionally, the EDS results indicate that P4 and P7 are mainly composed of Mg, Si, and O, which is similar to commonly occurring chrysotile (Figure 11), suggesting the conclusion of P4 and P7 as M–S–H having the structure of low-crystalline chrysotile. The characteristics (morphology, particle size, and SAED) of the M–S–H were similar to those of “proto-serpentine” which is a low-crystalline phase acting as a precursor to chrysotile in hydrothermal experiments by Lafay *et al.* (2016).

In summary, the above analyses may be seen to confirm present-day precipitation of M–S–H on the surface of the ultramafic rock mass. However, it is probably difficult for the precipitates to remain in this form on the surface of the ultramafic rock mass due to weathering and/or landslides. Therefore, precipitation of M–S–H likely occurs extremely rapidly compared with geological time scale.

Formation conditions and processes of magnesium silicate hydrates

The water chemistry in the studied sites is consistent with the water chemistry in ultramafic bodies in general, as reported by previous studies. Surface waters and seepage waters were essentially identified as Mg^{2+} – HCO_3^- type water (Figure 5), which Barnes and O’Neil (1969) and Barnes *et al.* (1978) characterized as a typical water chemistry of ultramafic bodies including serpentinite. Barnes and O’Neil (1969) mentioned that this water chemistry may be attributed to weathering phenomena with meteoric water. In the studied sites, meteoric water reacts with minerals (mainly serpentine) in ultramafic rock, generating alkaline water. Residence time of the groundwater is likely longer than surface water, which is suggested by the pH of the seepage water being slightly higher than that of the surface water (Table 1). Barnes and O’Neil (1969) also reported that Ca in solution is supplied from orthopyroxene. We collected the seepage sample from S2 with somewhat high Ca concentration (Table 1 and Figure 5). This sample indicates that the groundwater generating the seepage possibly had some interaction with orthopyroxene within the ultramafic body although orthopyroxene was not detectable in the XRD profiles of the collected bedrock samples from the surface of the outcrop (Figure 6).

To confirm the precipitation and discuss its conditions from the water chemistry, the chemical compositions of the liquid samples (surface waters and seepage waters from S1 and S2) were plotted in thermodynamic stability diagrams in the Mg–Si–H₂O, Ca–Si–H₂O, Mg–CO₂–H₂O, and Ca–CO₂–H₂O systems (Figure 12) obtained using The Geochemist’s Workbench (ver. 12; Bethke *et al.*, 2019) software with the Thermoddem database (Blanc *et al.*, 2012). The composition of M–S–H can be derived from two end-members (Mg/Si = 0.75 and 1.5; Nied *et al.*, 2016), thermodynamic data for these two types of M–S–H obtained from Lothenbach *et al.* (2019) were added to Thermoddem to consider them in the Mg–Si–H₂O system.

First, precipitation of M–S–H can also be expected from the thermodynamic calculations. The surface waters (S1-sf and S2-sf) are undersaturated with M–S–H at both S1 and S2, while the seepage waters (S1-sp and S2-sp) are oversaturated with M–S–H ($\text{M}_{1.5}\text{SH}_{2.5}$; Figure 12a). If S1-sf/S2-sf is mixed with S1-sp/S2-sp around S1/S2, the mixed solution (S1-mix/S2-mix) may be saturated with the M–S–H. Both sites show the surface water having higher activity of Si than the seepage water, and it may be assumed that mixing seepage with surface water would cause precipitation of M–S–H. This is consistent with the observation that precipitation occurred on the surface of the ultramafic rock mass at both S1 and S2 (Figure 3). Additionally, this thermodynamic discussion of $\text{M}_{1.5}\text{SH}_{2.5}$ is also consistent with the analyses of the solids, demonstrating that the M–S–H formed in the studied sites has a chrysotile-like crystal structure (Figures 7, 9 and 10) as $\text{M}_{1.5}\text{SH}_{2.5}$ (Mg/Si = 1.5) has been proposed to have a serpentine-like crystal structure, while $\text{M}_{1.5}\text{S}_2\text{H}_{2.5}$ (Mg/Si = 0.75) has been proposed to have a talc-like crystal structure (Nied *et al.*, 2016). No calcium silicate hydrate (C–S–H) would be expected to precipitate since all the water samples are undersaturated for C–S–H formations (Figure 12b).

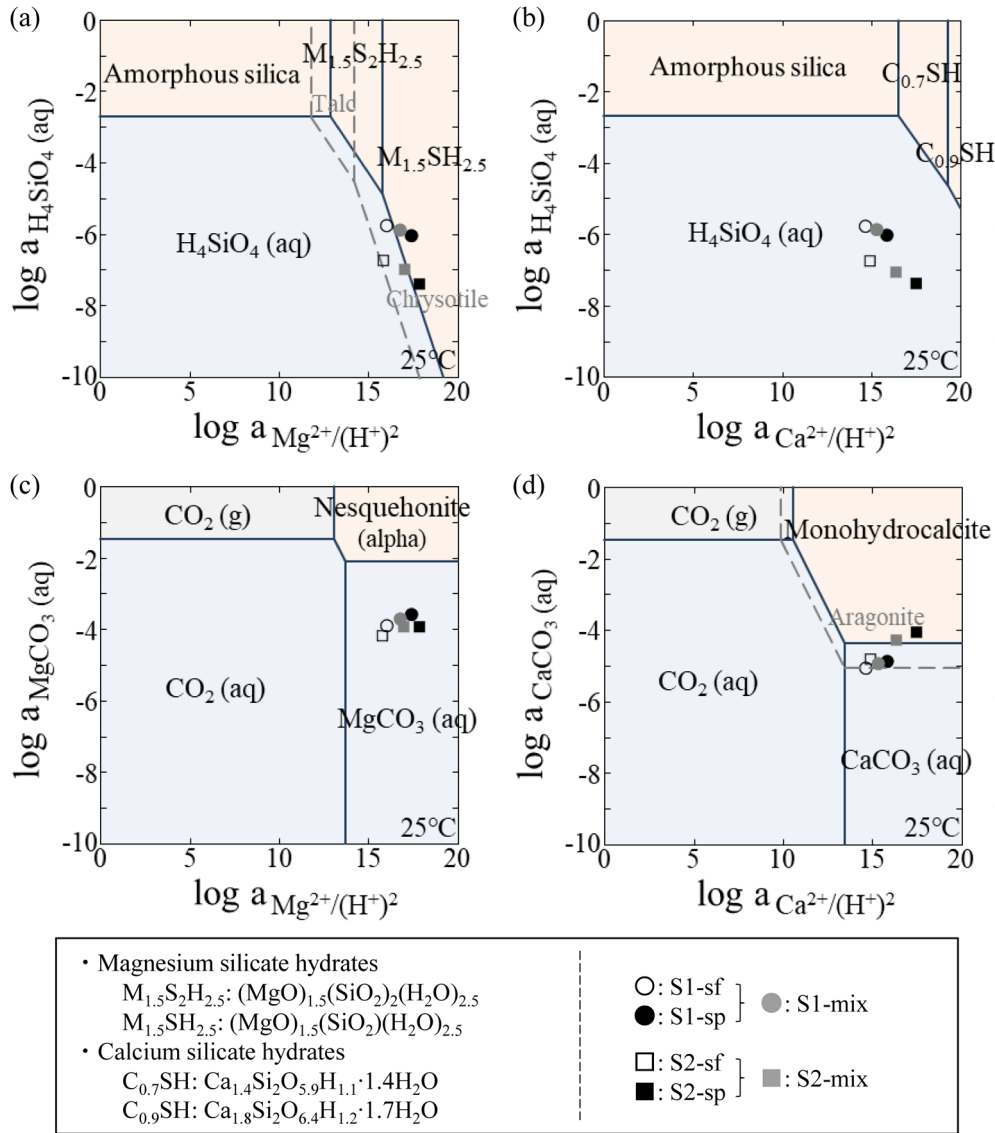


Fig. 12. Stability diagrams and thermodynamics of liquid samples in the (a) Mg–Si–H₂O system, (b) Ca–Si–H₂O system, (c) Mg–CO₂–H₂O system, and (d) Ca–CO₂–H₂O system at ambient temperature. Grayish solid symbols display 1 : 1 mixed solution of surface water and seepage water. Dotted lines show stability boundaries of talc and chrysotile in (a) and aragonite in (d).

Second, precipitation of carbonate minerals could also be expected by thermodynamic calculations. No Mg–carbonate mineral such as nesquehonite, which is a magnesium carbonate hydrate precipitated at ambient temperatures (Cheng *et al.*, 2009), can be expected to precipitate because of the undersaturation (Figure 12c). For aragonite, a Ca–carbonate mineral, the mixed solutions are oversaturated, and the saturation index of the mixed solution at S2 is much higher than that at S1 (Figure 12d). Further, the mixed solution at S2 is saturated with monohydrocalcite (Figure 12d). As aragonite easily forms under high saturation index conditions (Romanek *et al.*, 2011) or it may form *via* monohydrocalcite as a metastable precursor (Munemoto and Fukushi, 2008), the water chemistry of S2 may satisfy conditions for aragonite precipitation better than that of S1. This is consistent with the observation that aragonite is observed only with S2 (Figures 6 and 7d). Calcite is not considered in this calculation because dissolved Mg generally inhibits calcite formation (Kitano, 1962), something which is also supported by the absence

of calcite as determined in this study.

In summary, mixing of the solutions of surface waters and seepage waters induced the formation of M–S–H in both S1 and S2 and that of aragonite in S2. The M–S–H is likely formed because dissolved Mg preferentially binds to dissolved silica, and not to carbonate and hydroxide ions under the geochemical conditions of the studied sites. Tutolo and Tosca (2018) observed mineral paragenesis of M–S–H and aragonite in experiments around pH 10, which is consistent with the results of the solid analyses and thermodynamic calculations of the liquid samples in this study.

As discussed above, fluid mixing is an important factor to understand the geochemical processes of M–S–H formation at the sites studied. For the present study, we collected sediments on the surface of an ultramafic rock mass where landslides occur. The surface layer of the ultramafic rock mass contains much surface water derived from meteoric water, which is a factor contributing to the landslides. In this situation, precipitation is likely affected by both surface

water and seepage water. When seepage water merges with surface water displaying high activity of the dissolved Si, the mixed solution would induce the M–S–H formation, and consequently generate M–S–H on the surface of an ultramafic rock mass. This kind of fluid mixing for secondary mineral precipitation was also observed around alkaline springs on the Oman ophiolite by Anraku *et al.* (2017), and it does not appear to be in any way an extraordinary phenomenon around ultramafic regions.

Differences between magnesium silicate hydrates in laboratory experiments and in nature

Since previous studies on M–S–H have mostly been experimental studies, we will now discuss differences between the M–S–H reported in previous experimental studies and the M–S–H observed in this field survey. Some scientists have been analyzing M–S–H synthesized by experiments using reagents of MgO and SiO₂ with water/solid ratios ≤ 50 at around room temperature, and the XRD results showed four broad humps rather than distinct peaks (Zhang *et al.*, 2014; Roos *et al.*, 2015; Nied *et al.*, 2016; Bernard *et al.*, 2017). Furthermore, the *d*-values analyzed by XRD (4.5, 3.3, 2.6, and 1.5 Å) in the synthetic M–S–H from these studies are similar to some of those obtained from the SAED in TEM analysis of the natural M–S–H from this study (7.3, 4.5, 3.7, 2.5, 1.5, and 1.3 Å; Figures 9b and 10d). Results of the XRD and other analyses such as spectroscopy suggest that the experimental products have remarkably disordered and defective structures, which would indicate that the synthetic M–S–H samples are only poorly crystalline when compared with the M–S–H in this study, and that the synthetic M–S–H samples are somewhat different materials from the natural M–S–H samples. This is likely because the experiments were conducted in a closed system, and the saturation states of the dissolved Mg and Si in the experiments were much higher than those in nature. Taken together, the above facts suggest that while it is important to study M–S–H with synthetic samples, M–S–H must also be studied with natural samples when the purpose is an understanding of mineral–water interaction in the surface/subsurface geology. The characteristics of laboratory formed M–S–H may vary depending on conditions although M–S–H are essentially low-crystalline compounds composed of magnesium, silica, and water and precipitated at ambient temperatures.

It should also be noted that transformation of M–S–H possibly occurs after the primary precipitation of M–S–H. Although synthetic M–S–H samples are made under limited condition with respect to reaction time, some natural M–S–H samples may be transformed into more stable phases on geological time scales. The M–S–H in this study may act as a precursor of chrysotile and evolve into crystalline chrysotile even at ambient temperatures. In the stability diagram of a Mg–Si–H₂O system, the S1-mix and S2-mix are located in a stability field of M–S–H (M_{1.5}SH_{2.5}), which is essentially a location within a stability field of chrysotile (Figure 12a). Since the M–S–H in this study are low-crystalline chrysotile with nano-tubular particles, the M–S–H is possibly a metastable phase and the phase transformation from this M–S–H into chrysotile will proceed over long time scales.

Significance and implications of this study

This study would contribute to improvements in basic knowledge regarding present-day serpentinization at ambient temperatures. It is well known that the formation of chrysotile and other serpentine-group minerals (lizardite, antigorite, and others) are generally observed in conditions of high temperatures around mantle wedges or the lithosphere (O’Hanley, 1996). However, at ambient temperatures, we observed precipitation of an M–S–H (low-crystalline chrysotile), which has presumably been neglected due to X-ray amorphous. This suggests that where there is interaction of ultramafic rocks and alkaline fluids on the surface/subsurface of the Earth, some serpentinites may consist of M–S–H (and possibly crystalline serpentine generated by phase transformation from the M–S–H) as well as serpentine generated by ordinarily considered “serpentinization.” If geochemical settings on the surface of the Earth have alkaline fluids that show high Si activity and meets thermodynamic conditions for M–S–H formation, M–S–H easily precipitates even at ambient temperatures, which would be a commonly occurring phenomenon. Incidentally, recent studies have reported that serpentine and amorphous clay have also been observed on Mars (Ehlmann *et al.*, 2010; Hicks *et al.*, 2014). This suggests that precipitation of M–S–H and its transformation into chrysotile may have occurred even on the early Mars as well.

Further, this study may also provide significant implications for the engineering geology applications. For geological storage of CO₂, Mg–carbonate minerals have been considered as host phases for CO₂ trapping as well as Ca–carbonate. However, this study implies that the M–S–H phase should be considered to assess CO₂ storage capacity in geochemical systems including dissolved silica. For radioactive waste disposal in underground repositories, the previous experimental studies have identified M–S–H as a candidate for secondary phases in the engineered barriers with alkaline pore fluid (Ramirez *et al.*, 2002; Mäder *et al.*, 2017). While natural analogue studies with similar geochemical settings indicated the secondary phases are palygorskite (Mg–Al–silicates; Milodowski *et al.*, 2016) and smectite (Mg–Fe–silicates; Shimbashi *et al.*, 2018), we newly observed precipitation of M–S–H (mineralogically considered as low-crystalline chrysotile) in nature. To validate a mineral paragenesis model for long-term performance assessment of the engineered barriers, further studies need to clarify what geological factors influence the secondary mineral species.

CONCLUSIONS

We identified and verified the present-day precipitation of M–S–H on the surface of an ultramafic rock mass in the Kamukotan tectonic belt, Hokkaido, Japan. Sediments around seepage contained M–S–H that was likely precipitated at ambient temperatures on site and it was mineralogically identified as low-crystalline chrysotile, in addition to detrital serpentine from the bedrock. The M–S–H was different from commonly occurring chrysotile composing the bedrock with respect to morphology, particle size, and crystallinity while the chemical compositions were similar.

Precipitation of the M–S–H is influenced by seepage and

surface water around the studied sites. Seepage water merges with surface water having high activity levels of Si, making the mixed solution induce the M–S–H formation. Precipitation of M–S–H is presumably not an extraordinary phenomenon in natural Mg–Si–H₂O systems where geochemical settings are subjects to alkaline fluid that shows high Si activity and meets thermodynamic conditions for M–S–H formation. Furthermore, even in Mg–Ca–Si–CO₂–H₂O systems, M–S–H precipitates simultaneously with aragonite.

ACKNOWLEDGEMENTS

This study was supported financially by Grants-in-Aid for Scientific Research (A) (No. 19H00878) from the Japan Society for the Promotion of Science (JSPS) to T.S. and T.O. The TEM analysis was conducted at the Laboratory of Nano-Micro Material Analysis, supported by the “Nanotechnology Platform” of the Ministry of Education, Culture, Sports, Science and Technology (MEXT), Japan. We wish to thank Kosuke NAKAMURA (Faculty of Science, Hokkaido University) for preparation of polished sections, Ryohei KAWAKITA (Graduate School of Engineering, Hokkaido University) and Jhonard John GARCIA (National Institute of Geological Sciences, University of the Philippines Diliman) for assistance during the field survey, and anonymous reviewers for valuable comments to improve our manuscript.

REFERENCES

- ANRAKU, S., MATSUBARA, I., MORIMOTO, K., and SATO, T. (2017) Geochemical factors for secondary mineral formation at naturally-occurring hyperalkaline spring in Oman ophiolite. *Nendo Kagaku (Journal of the Clay Science Society of Japan)*, **55**, 17–30 (in Japanese with English abstract).
- ASAHINA, T. and KOMATSU, M. (1979) The Horokanai ophiolitic complex in the Kamuikotan tectonic belt, Hokkaido, Japan. *Chishitsugaku Zasshi*, **85**, 317–330.
- BARNES, I. and O’NEIL, J.R. (1969) The relationship between fluids in some fresh Alpine-type ultramafics and possible modern serpentinization, western United States. *Geological Society of America Bulletin*, **80**, 1947–1960.
- BARNES, I., O’NEIL, J.R., and TRESCASES, J.J. (1978) Present day serpentinization in New Caledonia, Oman and Yugoslavia. *Geochimica et Cosmochimica Acta*, **42**, 144–145.
- BERNARD, E., LOTHENBACH, B., RENTSCH, D., POCHARD, I., and DAUZÈRES, A. (2017) Formation of magnesium silicate hydrates (M–S–H). *Physics and Chemistry of the Earth*, **99**, 142–157.
- BETHKE, C.M., FARRELL, B., and YEAKEL, S. (2019) The Geochemist’s Workbench version 12. Aqueous Solutions LLC.
- BLANC, P., LASSIN, A., PIANTONE, P., AZAROUAL, M., JACQUEMET, N., FABBRI, A., and GAUCHER, E.C. (2012) Thermodden: A geochemical database focused on low temperature water/rock interactions and waste materials. *Applied Geochemistry*, **27**, 2107–2116.
- CHENG, W., LI, Z., and DEMOPOULOS, G.P. (2009) Effects of temperature on the preparation of magnesium carbonate hydrates by reaction of MgCl₂ with Na₂CO₃. *Chinese Journal of Chemical Engineering*, **17**, 661–666.
- DE RUITER, L. and AUSTRHEIM, H. (2018) Formation of magnesium silicate hydrate cement in nature. *Journal of the Geological Society*, **175**, 308–320.
- EHLMANN, B.L., MUSTARD, J.F., and MURCHIE, S.L. (2010) Geologic setting of serpentine deposits on Mars. *Geophysical Research Letters*, **37**, L06201.
- GEOLOGICAL SURVEY OF JAPAN (2019) Seamless Digital Geological Map of Japan (V2).
- HICKS, L.J., BRIDGES, J.C., and GURMAN, S.J. (2014) Ferric saponite and serpentine in the nakhlite martian meteorites. *Geochimica et Cosmochimica Acta*, **136**, 194–210.
- KATOH, T. and NAKAGAWA, M. (1986) Tectogenesis of ultramafic rocks in the Kamuikotan tectonic belt, Hokkaido, Japan. *Monograph of the Association for the Geological Collaboration in Japan*, **31**, 119–135 (in Japanese with English abstract).
- KITANO, Y. (1962) The behavior of various inorganic ions in the separation of calcium carbonate from a bicarbonate solution. *Bulletin of the Chemical Society of Japan*, **35**, 1973–1980.
- KONTOYANNIS, C.G. and VAGENAS, N.V. (2000) Calcium carbonate phase analysis using XRD and FT-Raman spectroscopy. *Analyst (London)*, **125**, 251–255.
- LAFAY, R., FERNANDEZ-MARTINEZ, A., MONTES-HERNANDEZ, G., AUZENDE, A.L., and POULAIN, A. (2016) Dissolution–reprecipitation and self-assembly of serpentine nanoparticles preceding chrysotile formation: Insights into the structure of proto-serpentine. *The American Mineralogist*, **101**, 2666–2676.
- LOTHENBACH, B., KULIK, D.A., MATSCHEL, T., BALONIS, M., BAQUERIZO, L., DILNESA, B., MIRON, G.D., and MYERS, R.J. (2019) Cemdata18: A chemical thermodynamic database for hydrated Portland cements and alkali-activated materials. *Cement and Concrete Research*, **115**, 472–506.
- MÄDER, U., JENNI, A., LEROUGE, C., GABOREAU, S., MIYOSHI, S., KIMURA, Y., CLOET, V., FUKAYA, M., CLARET, F., Otake, T., SHIBATA, M., and LOTHENBACH, B. (2017) 5-year chemico-physical evolution of concrete–claystone interfaces, Mont Terri rock laboratory (Switzerland). *Swiss Journal of Geosciences*, **110**, 307–327.
- MATSUSHITA, H., MARUYAMA, H., AOMI, T., and ISHIKAWA, N. (1974) Silver–silver chloride electrode prepared with the use of molten silver chloride. *Memoirs of Chubu Institute of Technology*, **10-A**, 117–122.
- MILODOWSKI, A.E., NORRIS, S., and ALEXANDER, W.R. (2016) Minimal alteration of montmorillonite following long-term interaction with natural alkaline groundwater: implications for geological disposal of radioactive waste. *Applied Geochemistry*, **66**, 184–197.
- MUNEMOTO, T. and FUKUSHI, K. (2008) Transformation kinetics of monohydrocalcite to aragonite in aqueous solutions. *Journal of Mineralogical and Petrological Sciences*, **103**, 345–349.
- NIED, D., ENEMARK-RASMUSSEN, K., HOPITAL, E.L., SKIBSTED, J., and LOTHENBACH, B. (2016) Properties of magnesium silicate hydrates (M–S–H). *Cement and Concrete Research*, **79**, 323–332.
- NINOMIYA, J., MIZUOCHI, Y., KATOH, T., OKAMOTO, M., and YAJIMA, T. (2007) CO₂ fixation in the serpentinite-groundwater system. *Nendo Kagaku (Journal of the Clay Science Society of Japan)*, **46**, 28–32 (in Japanese with English abstract).
- NOZAWA, S., SATO, T., and Otake, T. (2018) Effect of dissolved silica on immobilization of boron by magnesium oxide. *Minerals (Basel)*, **8**, 76.
- O’HANLEY, D.S. (1996) *Serpentinities: Records of Tectonic and Petrological History*. Oxford University Press, New York.
- OKAMOTO, I., MIZUOCHI, Y., NINOMIYA, A., KATO, T., YAJIMA, T., and OHSUMI, T. (2006) In-situ test on CO₂ fixation by serpentinite rock mass in Japan. *8-th International Conference of Greenhouse Gas Control Technologies*, Trondheim, Norway.
- OLAJIRE, A.A. (2014) Review of ASP EOR (alkaline surfactant polymer enhanced oil recovery) technology in the petroleum industry: Prospects and challenges. *Energy*, **77**, 963–982.
- OWADA, A., SATO, T., HIRABAYASHI, E., NAGAYOSHI, K., and SUZUKI, M. (2014) Japan Patent Kokai, 5633078.
- RAMIREZ, S., CUEVAS, J., VIGIL, R., and LEGUEY, S. (2002) Hydrothermal alteration of “La Serrata” bentonite (Almería, Spain) by alkaline solutions. *Applied Clay Science*, **21**, 257–269.
- RINAUDO, C., GASTALDI, D., and BELLUSO, E. (2003) Characterization of chrysotile, antigorite and lizardite by FT-Raman spectroscopy. *Canadian Mineralogist*, **41**, 883–890.
- ROMANEK, C.S., MORSE, J.W., and GROSSMAN, E.L. (2011) Aragonite kinetics in dilute solutions. *Aquatic Geochemistry*, **17**, 339–356.
- ROOSZ, C., GRANGEON, S., BLANC, P., MONTOUILLOUT, V., LOTHENBACH, B., HENOCQ, P., GIFFAUT, E., VIEILLARD, P., and GABOREAU, S. (2015) Crystal structure of magnesium silicate hydrates (M–S–H): The relation with 2:1 Mg–Si phyllosilicates. *Cement and Concrete Research*, **73**, 228–237.
- ROUNDS, S.A. (2012) Alkalinity and acid neutralizing capacity. In: *Techniques of Water-Resources Investigations Book 9, Chap. A6* (F.D. Wilde, editor). United States Geological Survey, Reston, Virginia.
- SHIMBASHI, M., SATO, T., YAMAKAWA, M., FUJII, N., and Otake, T. (2018) Formation of Fe- and Mg-rich smectite under hyperalkaline conditions at Narra in Palawan, the Philippines. *Minerals (Basel)*, **8**, 155.
- TOSCA, N.J. and MASTERSON, A.L. (2014) Chemical controls on incipient

- Mg–silicate crystallization at 25°C: Implications for early and late diagenesis. *Clay Minerals*, **49**, 165–194.
- TUTOLO, B.M. and TOSCA, N.J. (2018) Experimental examination of the Mg–silicate–carbonate system at ambient temperature: Implications for alkaline chemical sedimentation and lacustrine carbonate formation. *Geochimica et Cosmochimica Acta*, **225**, 80–101.
- UEDA, H. (2005) Accretion and exhumation structures formed by deeply subducted seamounts in the Kamuikotan high-pressure/temperature zone, Hokkaido, Japan. *Tectonics*, **24**, 1–17.
- UMAR, A.A. and SAAID, I.B.M. (2013) Silicate scales formation during ASP flooding: A review. *Research Journal of Applied Sciences, Engineering and Technology*, **6**, 1543–1555.
- WADA, K. (1989) Allophane and imogolite. Pp. 1051–1087 in: *Minerals in Soil Environments*, 2nd edition (J.B. Dixon and S.B. Weed, editors). Soil Science Society of America, Madison, Wisconsin.
- WICKS, F.J. and O'HANLEY, D.S. (1988) Serpentine minerals: Structure and petrology. Pp. 91–159 in: *Hydrous Phyllosilicates* (S.W. Bailey, editor). Reviews in Mineralogy, 19, Mineralogical Society of America, Washington, D.C.
- YADA, K. (1979) Microstructure of chrysotile and antigorite by high-resolution electron microscopy. *Canadian Mineralogist*, **17**, 679–691.
- ZHANG, T., VANDEPERRE, L.J., and CHEESEMAN, C.R. (2014) Cement and Concrete Research Formation of magnesium silicate hydrate (M–S–H) cement pastes using sodium hexametaphosphate. *Cement and Concrete Research*, **65**, 8–14.
- ZHUANG, Y., YANG, Y., XIANG, G., and WANG, X. (2009) Magnesium silicate hollow nanostructures as highly efficient absorbents for toxic metal ions. *The Journal of Physical Chemistry C*, **113**, 10441–10445.
- ZUSSMAN, J., BRINDLEY, G.W., and COMER, J.J. (1957) Electron diffraction studies of serpentine minerals. *The American Mineralogist*, **42**, 133–153.

(Manuscript handled by Tetsuichi Takagi)